The Astrophysical Journal, 849:52 (7pp), 2017 November 1 https://doi.org/10.3847/1538-4357/aa8e43

Enhanced Polarized Emission from the One-parsec-scale Hotspot of 3C 84 as a Result of the Interaction with the Clumpy Ambient Medium

H. Nagai[1,2], Y. Fujita[3], M. Nakamura[4], M. Orienti[5,6], M. Kino[1,7], K. Asada[4], and G. Giovannini[5,6]
[1] National Astronomical Observatory of Japan, Osawa 2-21-1, Mitaka, Tokyo 181-8588, Japan; hiroshi.nagai@nao.ac.jp
[2] The Graduate University for Advanced Studies (SOKENDAI), Osawa 2-21-1, Mitaka, Tokyo 181-8588, Japan
[3] Theoretical Astrophysics, Department of Earth and Space Science, Graduate School of Science, Osaka University, 1-1 Machikaneyama-cho, Toyonaka, Osaka 560-0043, Japan
[4] The Academia Sinica Institute of Astronomy and Astrophysics, AS/NTU. No.1, Section 4, Roosevelt Road, Taipei 10617, Taiwan, R.O.C.
[5] Instituto di Radioastronomia, Via P. Gobetti, 101, I-40129 Bologna, Italy
[6] Dipartimento di Fisica e Astronomia, Universita' di Bologna, via Gobetti 83b, I-40129 Bologna, Italy
[7] Kogakuin University, Academic Support Center, 2665-1 Nakano, Hachioji, Tokyo 192-0015, Japan
Received 2017 July 24; revised 2017 September 5; accepted 2017 September 19; published 2017 October 30

Abstract

We present Very Long Baseline Array polarimetric observations of the innermost jet of 3C 84 (NGC 1275) at 43 GHz. A significant polarized emission is detected at the hotspot of the innermost restarted jet, which is located 1 pc south from the radio core. While the previous report presented a hotspot at the southern end of the western limb, the hotspot location has been moved to the southern end of the eastern limb. Faraday rotation is detected within an entire bandwidth of the 43 GHz band. The measured rotation measure (RM) is at most $(6.3 \pm 1.9) \times 10^5$ rad m^{-2} and might be slightly time variable on the timescale of a month by a factor of a few. Our measured RM and the RM previously reported by the CARMA and SMA observations cannot be consistently explained by the spherical accretion flow with a power-law profile. We propose that a clumpy/inhomogeneous ambient medium is responsible for the observed RM. Using an equipartition magnetic field, we derive the electron density of 2×10^4 cm^{-3}. Such an electron density is consistent with the cloud of the narrow line emission region around the central engine. We also discuss the magnetic field configuration from the black hole scale to the parsec scale and the origin of low polarization.

Key words: galaxies: active – galaxies: individual (3C 84, NGC 1275, Perseus A) – galaxies: jets – radio continuum: galaxies

1. Introduction

3C 84 is associated with the giant elliptical galaxy NGC 1275 ($z = 0.0176$), whose nuclear emission is classified as a Seyfert 1.5/LINER (Sosa-Brito et al. 2001), centered at the Perseus cluster. The total luminosity is 4×10^{44} erg s^{-1} (Levinson et al. 1995). This luminosity is about 0.4% of the Eddington luminosity for a black hole mass of $8 \times 10^8 M_\odot$ (Scharwächter et al. 2013). The radio luminosity of this source is 3×10^{24} W Hz^{-1} sr^{-1} at 178 MHz, which is classified as a Fanaroff–Riley I radio source (Fanaroff & Riley 1974). The radio morphology is quite complex. Multiple radio lobes are found on different angular scales, suggesting intermittent radio jet activities. The most recent jet activity started in ∼2005 (Nagai et al. 2010; Suzuki et al. 2012). The restarted jet extends up to ∼1 pc to the south from the core and a hotspot and lobe-like structure are formed at the southern end (e.g., Nagai et al. 2014). The counter jet has also recently been discovered (Fujita & Nagai 2017). Based on the jet-counter jet ratio, Fujita & Nagai (2017) estimated that the jet forms an angle of $65° \pm 15°$ with the line of sight, which is similar to the one for the jet associated with the previous episode of activity (e.g., Asada et al. 2006). The total radio flux density is about 40 Jy at 10 GHz.[8] Most of the radio emissions originate in the innermost jet.[9]

NGC 1275 has been the subject of extensive studies of the circumnuclear gas properties in connection with the mass accretion onto the super massive black hole (SMBH). NGC 1275 is known to have a large reservoir of cold molecular gas (Salomé et al. 2006; Lim et al. 2008) in contrast to the other brightest cluster galaxies (BCGs) such as M87 (Perlman et al. 2007; Tan et al. 2008). The total amount of molecular gas mass ($M_{\rm gas}$) is $M_{\rm gas} \simeq 10^{10} M_\odot$. A large fraction of this molecular gas is located within the central 1 kpc ($M_{\rm gas} \simeq 10^9 M_\odot$: Lim et al. 2008). In the inner 50 pc, the circumnuclear disk (CND) is resolved by the warm H_2 and ionized [Fe II] lines, both in morphology and kinematics with the Gemini North Telescope (Scharwächter et al. 2013). It was suggested from the observed velocity dispersion that the H_2 emission traces the outer region of the disk, which is likely to form a toroid, while the [Fe II] line traces the inner region of the disk illuminated by the ionizing photons from the active galactic nucleus (AGN). The inner ionized part is possibly associated with the "silhouette" disk, which was identified by the free–free absorption (FFA) of background synchrotron emission from the counter jet by VLBI observations (Romney et al. 1995; Walker et al. 2000).

The intermittent jet activity of 3C 84 indirectly predicts that the accretion flow is strongly inhomogeneous. Numerical simulations of giant elliptical galaxies suggest that the mass accretion is dominated by chaotic cold accretion within the inner kiloparsecs (Gaspari et al. 2013). The simulations also predict that the chaotic cold accretion leads to a deflection of jets and strong variation in the AGN luminosity. Such a jet deflection and luminosity change are indeed observed in NGC 1275/3C 84 in radio, X-ray, and γ-ray bands (Nagai et al. 2010; Dutson et al. 2014; Fabian et al. 2015).

[8] F-GAMMA program: http://www3.mpifr-bonn.mpg.de/div/vlbi/fgamma/fgamma.html.
[9] MOJAVE program: http://www.physics.purdue.edu/MOJAVE/index.html.

Fujita & Nagai (2017) measured the opacity of FFA ($\tau_{\rm ff}$) toward the counter jet component on the central ~1 pc region and found $\tau_{\rm ff} \propto \nu^{-0.6}$, which is different from the one for a uniform density of $\tau_{\rm ff} \propto \nu^{-2}$. They argued that the absorbing medium is highly inhomogeneous and that it consists of regions of $\tau_{\rm ff} \ll 1$ and $\tau_{\rm ff} \gg 1$.

Recently, VLBA images at 43 GHz from the Boston University Blazar Program[10] have pointed out an enhancement of the polarized emission at the hotspot of the innermost jet as well as the abrupt change in its position. At the beginning of 2013, the hotspot was located along the western limb (Nagai et al. 2014). This situation was not changed until the middle of 2015. After that, the hotspot on the western limb became less obvious, and the hotspot appeared at the eastern limb until the middle of 2016, accompanied by the polarized emission. In more recent data, the hotspot structure has even become distorted. These behaviors suggest a strong interaction between the jet and ambient medium. The enhancement of the polarized emission is an important tool to probe the ambient medium on parsec scales. In this paper, we report the analysis of the total and polarized intensities in five epochs between 2015 December and 2016 April as well as Faraday rotation measure (RM) along the line of sight toward the polarized emission, which can constrain the electron density of the ambient medium. Throughout this paper, we use $H_0 = 70.5$, $\Omega_{\rm M} = 0.27$, and $\Omega_\Lambda = 0.73$. At the 3C 84 distance, 1 mas corresponds to 0.344 pc.

2. Data

We used the calibrated VLBA archival data taken as the part of Boston University Blazar Program. The observations were done on 2015 December 05, 2016 January 01, 2016 January 31, 2016 March 18, and 2016 April 22 at 43 GHz with 10 VLBA stations. The data consist of four intermediate frequencies (IFs) with a 64 MHz bandwidth for each IF. The central frequencies of each band are 43.008, 43.087, 43.151, and 43.215 GHz for IF 1, 2, 3, and 4, respectively. The total bandwidth is 256 MHz per polarization. Both right-hand (R) and left-hand (L) circular polarizations were received, and RR, LL, RL, and LR correlations were obtained. The calibrations were done in the same manner as describe in Jorstad et al. (2005). The instrumental polarizations (D-terms) were derived by averaging values over t13 sources observed in each epoch in each IF using AIPS task LPCAL. The absolute electric vector position angle (EVPA) calibration was done with the D-term method (Gómez et al. 2002) and using jet features with stable EVPAs in several quasars.

The imaging was done using the CLEAN algorithm implemented in Difmap software (Shepherd et al. 1994). Each IF is imaged separately in Stokes I, Q, and U. Figures 1(a)–(e) show the total and polarized intensity images. A bright and compact region, which is consistent with a hotspot, is clearly detected at the position of ~3 mas from the core along the eastern limb. In Figure 1(f), we also show the total intensity image in 2013 when the hotspot was seen on the western limb as a comparison.

The peak polarized intensity, EVPA, and polarization percentage are tabulated in Table 1. The errors of polarized intensity and EVPA are calculated from image rms on Stokes Q and U.

[10] http://www.bu.edu/blazars/VLBAproject.html

3. Results

The polarized emission is clearly detected on the hotspot throughout all epochs at the level of 1%–3% (Table 1). Significance levels are about 5σ in 2015 December 05 and more than 7σ in the rest of the epochs. In general, the polarization debias should be taken into account (Vaillancourt 2006), but the signal-to-noise ratio is very high, and thus the debiased value of the polarized intensity is unchanged to within the uncertainty of the original value. The main polarization feature on the hotspot is very compact and its location is not largely changed throughout these epochs. In addition to this main polarization feature, some extended polarized emissions are detected around the hotspot in 2016 March 18 and 2016 April 22.

Figure 2 shows the polarization position angle of the main polarized feature as a function of wavelength square. The polarization position angle is computed from Stokes Q and U intensities at the polarized peak position. The rotation of EVPA with frequency is clearly detected except for data on 2016 April 22. The inferred Faraday RM is an order of 10^5 rad m^{-2} (Table 2). This level of RM is about two orders of magnitude higher than the one reported on the polarization feature detected on the ~10 mas scale radio lobe in 2004 (Taylor et al. 2006), which is associated with the previous episode of jet activity. The same order of RM is also reported by millimeter interferometric observations in 2011–2013 (Plambeck et al. 2014). The RM might be slightly time variable (see Figure 2 and Table 2).

The most intriguing finding is that the EVPA after the correction of Faraday rotation changes abruptly on the timescale of a month (see Table 2), which is the evidence of rapid change in the projected magnetic field direction at the hotspot. Given that the relative position of the main polarized feature to the core is almost unchanged, the change in the magnetic field direction requires that the size of the feature is smaller than one light month.

4. Discussion and Conclusions

4.1. Hotspot

The polarized emission from the hotspot was not clearly detected before the middle of 2015 when the hotspot was observed on the western limb (Nagai et al. 2014, see also the webpage of the Boston University Blazar Program). After the hotspot recently appeared on the eastern limb, the polarized emission was suddenly enhanced. This hotspot movement as well as the enhancement of the polarized emission presumably indicates that the jet is jittering in an inhomogeneous ambient medium, which results in the movement of the termination shock. Similar behavior of hotspots is predicted by recent numerical simulations where the jet beam is injected in the dense inhomogeneous ambient medium (e.g., Wagner et al. 2012). Alternatively, the ejection of jet flows that represents the eastern and western limb structures could be time variable and nonsimultaneous between two limbs.

For a simple transverse shock, the magnetic field becomes perpendicular to the jet with an enhancement of fractional polarization due to the shock compression (Laing 1980). However, the Faraday-rotation-corrected position angle indicates that the projected magnetic field is not always perpendicular to the jet axis (see Table 2). There is no strong correlation between the fractional polarization and the project

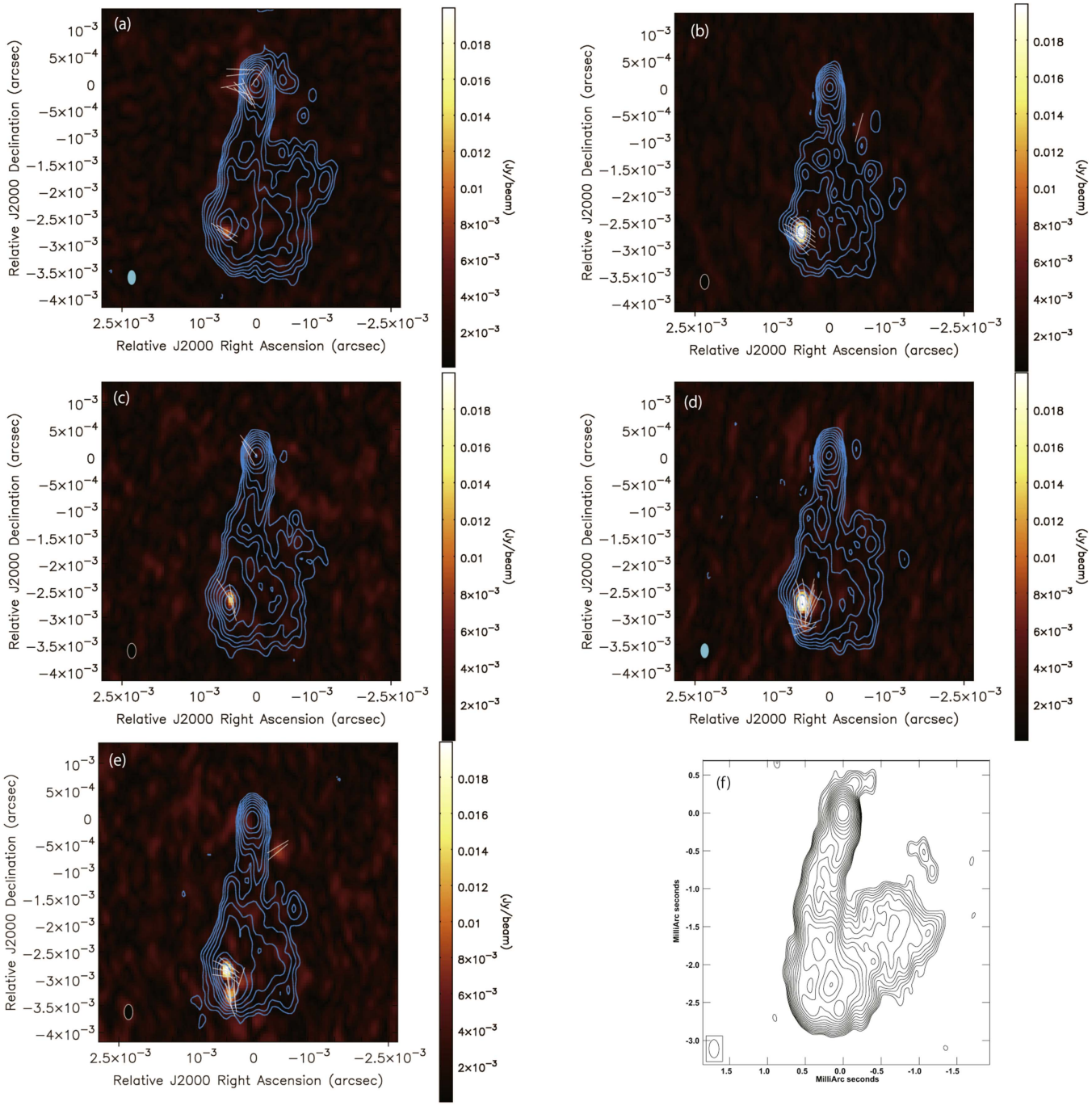

Figure 1. VLBA images of 3C 84 on (a) 2015 December 05, (b) 2016 January 01, (c) 2016 January 31, (d) 2016 March 18, and (e) 2016 April 22. Total intensity is indicated by cyan contours overlaid on the polarized intensity in color. Total intensity images are made by combining all four IFs, while the polarized intensity is for IF1. The 1σ of the total intensities are 1.67, 5.56, 3.55, 3.99, and 4.44 mJy on 2015 December 05, 2016 January 01, 2016 January 31, 2016 March 18, and 2016 April 22, respectively. The contour levels are plotted at the level of $(-1, 1, 2, 4, ..., 2048) \times 3\sigma$ of each image. The polarization position angles are indicated by the white vectors, which are shown on the area where the polarized intensity is greater than 3σ of the polarized intensity images. The restoring beam size is (0.28×0.16) mas at a position angle of 0°. (f) The 43 GHz VLBA image of 3C 84 in 2013 January 24, which is the same image shown in Nagai et al. (2014).

magnetic field direction. Thus, the source of polarized emission in the hotspot of 3C 84 is presumably not only dominated by a simple transverse shock.

Variations in the projected magnetic field are seen on the timescale of a month, which constrains the cross-sectional size of the hotspot to be less than one light month (∼0.07 mas). This upper limit of the size can be roughly interpreted as the width of the eastern jet limb since the hotspot is observed on the eastern limb. The jet limb is not well resolved even in the recent space VLBI image with the Radioastron (beam size ∼0.05 mas, G. Giovannini et al. 2017, in preparation), which seems to be consistent with this picture.

4.2. Origin of Faraday Screen

Faraday rotation can occur in any magnetized plasma along the line of sight between the source and the observer in general. However, we can naturally expect that the observed Faraday rotation originates close to the nucleus of 3C 84, as discussed

Table 1
Polarization Properties of the Hotspot

Date	Freq. (GHz)	P (mJy)[a]	χ (degree)[b]	F (%)[c]
2015 Dec 05	43.007	10.2 ± 1.8	66.3 ± 7.1	1.28 ± 0.23
	43.087	9.7 ± 2.1	61.7 ± 8.6	1.21 ± 0.26
	43.151	11.2 ± 1.8	59.7 ± 6.4	1.40 ± 0.23
	43.215	11.0 ± 1.8	58.9 ± 6.2	1.37 ± 0.22
2016 Jan 01	43.007	33.2 ± 1.6	63.2 ± 2.0	2.10 ± 0.10
	43.087	34.3 ± 1.6	56.3 ± 1.9	2.21 ± 0.10
	43.151	31.7 ± 2.1	56.9 ± 3.0	2.05 ± 0.14
	43.215	35.6 ± 1.8	50.0 ± 2.1	2.30 ± 0.12
2016 Jan 31	43.008	15.0 ± 2.0	14.5 ± 5.4	1.02 ± 0.14
	43.087	16.8 ± 2.2	12.1 ± 5.3	1.14 ± 0.15
	43.151	15.7 ± 2.3	0.0 ± 6.2	1.07 ± 0.16
	43.215	14.1 ± 2.3	0.0 ± 6.4	0.86 ± 0.15
2016 Mar 18	43.008	30.8 ± 2.1	10.7 ± 2.6	1.08 ± 0.08
	43.087	33.8 ± 2.2	12.2 ± 2.4	1.19 ± 0.08
	43.151	33.0 ± 2.1	0.0 ± 2.6	1.16 ± 0.08
	43.215	34.6 ± 2.1	0.0 ± 2.3	1.21 ± 0.07
2016 Apr 22	43.008	24.2 ± 2.5	69.2 ± 4.2	0.92 ± 0.10
	43.087	20.0 ± 2.7	66.2 ± 5.5	0.76 ± 0.10
	43.151	23.7 ± 2.7	73.2 ± 4.6	0.90 ± 0.10
	43.215	20.0 ± 2.7	64.0 ± 5.5	0.76 ± 0.10

Notes.
[a] Observed polarization position angle.
[b] Observed polarization position angle.
[c] Polarization percentage.

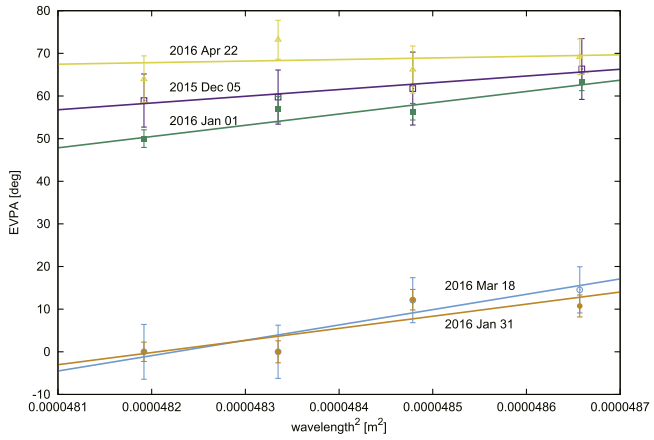

Figure 2. EVPA as a function of wavelengths squared.

Table 2
Faraday Rotation Measure on the Polarized Feature

Date	Rotation measure (rad m^{-2})	χ_0 (degree)[a]
2015 Dec 05	$(2.7 \pm 0.5) \times 10^5$	-23 ± 5
2016 Jan 01	$(4.6 \pm 0.9) \times 10^5$	89 ± 19
2016 Jan 31	$(6.3 \pm 1.9) \times 10^5$	30 ± 10
2016 Mar 18	$(5.0 \pm 2.2) \times 10^5$	24 ± 11
2016 Apr 22	$<2.3 \times 10^5$	N/A

Note.
[a] Faraday-rotation-corrected EVPA.

in Plambeck et al. 2014). Taylor et al. reported the RM of 7000 rad m^{-2} on the southern jet/lobe separated from the core by ∼8 pc. Our measured RM on the hotspot separated from the core by ∼1 pc is at most two orders of magnitude higher than this, and thus the Faraday screen, which is responsible for the RM of $\sim 10^5$ rad m^{-2}, should originate in 1 pc $< r <$ 8 pc in the projected distance (r is the distance from the core). We note that the projection effect is not very significant in the estimation of distance since the jet angle to the line of sight is moderate ($65 \pm 16°$: Fujita & Nagai 2017). The jet angle is also independently estimated by the modeling of the broadband spectrum from radio to γ-ray using synchrotron self-Compton (SSC) with some external photons, which favors smaller angles (e.g., 18°: Tavecchio & Ghisellini 2014). If this is the case, the hotspot distance is larger by a factor of a few.

The bolometric luminosity of 3C 84 is about 0.4% of the Eddington luminosity. Thus, the accretion flow of 3C 84 is likely to be a radiatively inefficient accretion flow (RIAF: Narayan & Yi 1995) rather than a standard disk (Shakura & Sunyaev 1973). However, we note that 3C 84 has a cold ($T_e \sim 10^4$ K) disk-like accretion flow, as identified by FFA of the emission from the counter jet in the parsec scale (Walker et al. 2000) and inhomogeneous gas distribution around the black hole (Fujita et al. 2016). A number of theoretical studies predicted that the accretion flow components of hot geometrically thick (RIAF-like) and cold geometrically thin can coexist in either horizontal or vertical stratification (e.g., Miller & Stone 2000; Merloni & Fabian 2002; Liu et al. 2007; Ho 2008; Liu & Taam 2013). The measured Faraday rotation can be caused by such an RIAF-like component. We thus estimate the accretion rate of the RIAF-like component using the measured RM. For a simplicity, we assume that the RIAF-like component is a quasi-spherical Bondi accretion flow with a power-law density profile. We can calculate the accretion rate, following the formulation as follows (Quataert & Gruzinov 2000; Marrone et al. 2006; Kuo et al. 2014).

$$\dot{M} = 1.3 \times 10^{-10}[1 - (r_{\rm out}/r_{\rm in})^{-(3\beta-1)/2}]^{-2/3} \times \left(\frac{M_{\rm BH}}{8.0 \times 10^8 M_\odot}\right)^{4/3} \left(\frac{2}{3\beta - 1}\right)^{-2/3} r_{\rm in}^{7/6} \left(\frac{\rm RM}{\rm rad\ m^{-2}}\right)^{2/3}.$$

For an inner effective radius $r_{\rm in}$ of 1 pc ($1.3 \times 10^4 R_s$), where the hotspot is located, the observed RM implies an accretion rate of $\sim 4.3 \times 10^{-2} M_\odot$ yr^{-1} and $\sim 8.6 \times 10^{-2} M_\odot$ yr^{-1} for $\beta = 0.5$ and $\beta = 1.5$, which are corresponding to convection-dominated accretion flow (CDAF: Narayan et al. 2000; Quataert & Gruzinov 2000) and advection-dominated accretion flow (ADAF: Ichimaru 1977; Narayan & Yi 1995), respectively. Here we assumed the outer effective radius $r_{\rm out}$ of $10^5 R_s$ (∼8 pc), which is approximately the same with the Bondi radius of 8.6 pc (Fujita et al. 2016). The derived accretion rate is roughly consistent with that estimated from the bolometric luminosity with a black hole mass of $8 \times 10^8 M_\odot$ and a radiative efficiency of 10% ($\dot{M} \sim L_{\rm bol}/(0.1c^2) \simeq 7.1 \times 10^{-2} M_\odot$ yr^{-1}).

Plambeck et al. (2014) also reported the detection of the polarized emission at 210–345 GHz with the CARMA and SMA. The RM is measured to be $\sim 9 \times 10^5$ rad m^{-2}, which agrees with the largest RM in our measurements (6×10^5 rad m^{-2}) within a factor of two. They also estimated the accretion rate using the same method mentioned above and found that the derived accretion rate is much smaller than the one expected from the bolometric luminosity of 3C 84. In this calculation, they assumed that the polarized emission originates in a small region at the vicinity of the black hole since the emission from the inner jet can be dominant in shorter wavelengths (e.g., Lobanov 1998;

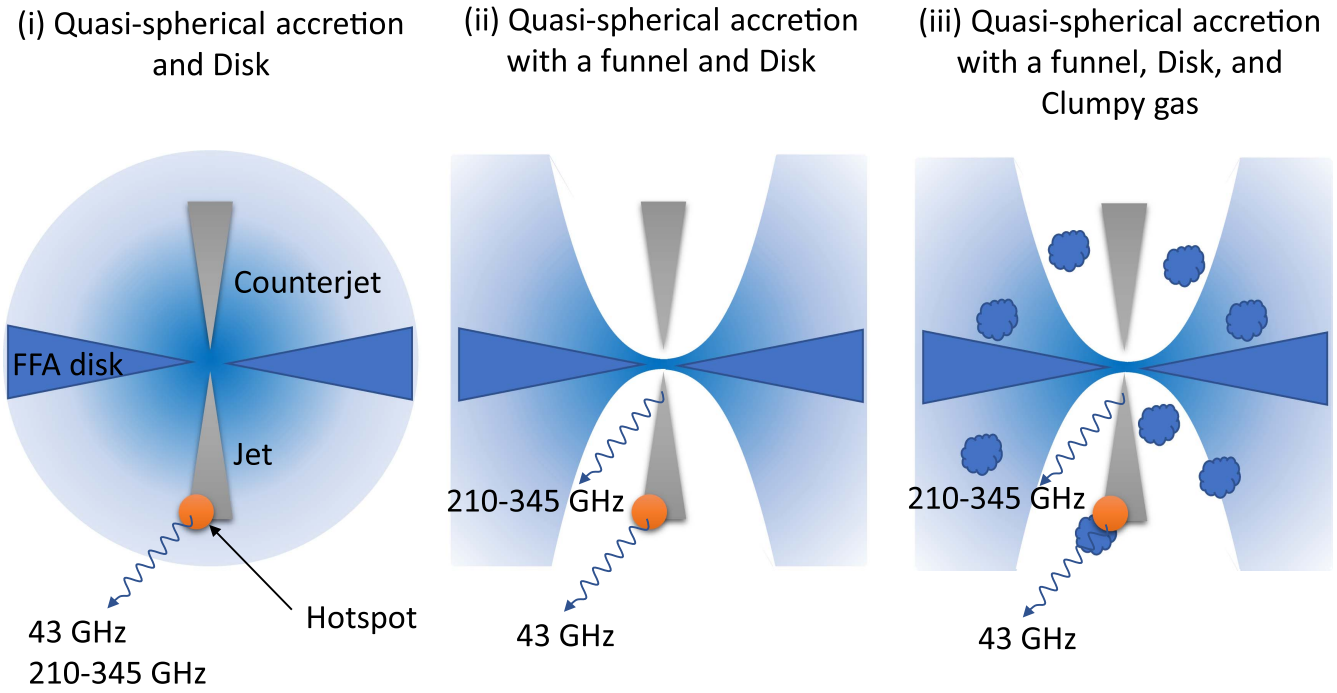

Figure 3. Schematic image of possible accretion flow structures. (i) 210–345 GHz emission is dominant in the hotspot. Faraday rotation is caused by RIAF. (ii) 210–345 GHz emission is dominant in the inner jet. Funnel zones are created by the previous jet activities, which causes a decrease of Faraday rotation as compared to case (i). (iii) The jet is interacting with a clumpy gas, which is responsible for the observed Faraday rotation toward the hotspot at 43 GHz.

Hada et al. 2011; Sokolovsky et al. 2011). One possible explanation is that the emission does not dominate at the inner jet but at the hotspot, even at 210–345 GHz (see Figure 3(i)). However, one problem with this hypothesis is that the polarized flux measured by Plambeck et al. is too large to be attributable to the emission from the hotspot. They reported about 1.5% of the polarization percentage in 2011–2013. Given that the total flux was 6–8 Jy in this period, the polarization flux was estimated to be about 100 mJy. On the other hand, our measured integrated polarized flux is at most 30 mJy, and it seems to be difficult to connect these two data sets unless the hotspot spectrum is inverted. Thus, the polarized emission detected with CARMA and SMA seems to originate in a place that is different from the one from the hotspot. Consequently, a simple quasi-spherical accretion flow (Figure 3) cannot be applied to NGC 1275.

The underprediction of RM by the CARMA and SMA observations indicates the necessity of reducing the accretion rate within 1 pc. One possibility is that a part of the accretion flow is blown out by the jet and hollow "funnels" are formed parallel to the jet axis (see Figure 3(ii)). Since 3C 84 shows intermittent jet activities, the jet of previous activity can blow out the gas of the accretion flow. The jets of ongoing activity are probably passing through the inflating "cocoon" filled by the shocked jet material (Begelman & Cioffi 1989) of the previous jet activity. Such a cocoon can be identified as emissions at lower frequencies (Taylor & Vermeulen 1996; Silver et al. 1998; Walker et al. 2000), which indicates that a certain amount of relativistic plasma fills the cocoon. Faraday rotation is weakened in relativistic plasma by a factor of $\ln \gamma/2\gamma^2$, where γ is electron Lorentz factor (Quataert & Gruzinov 2000). Thus, we may ignore the effect of Faraday rotation within the cocoon. The cocoon may also explain the observed jet collimation. Nagai et al. (2014) found a rather cylindrical collimation of the jet on a subparsec scale, while the power-law density profile of the ambient medium, which is expected from RIAF models, predicts a jet collimation of the parabolic profile (e.g., Narayan & Fabian 2011). The observed collimation profile can be maintained by a strong pressure of the hot cocoon.

With this configuration of accretion flow (Figure 3(ii)), however, the RM observed toward the hotspot can also be smaller than the case for the simple spherical accretion flow (Figure 3(i)). We need an additional component to account for the observed RM toward the hotspot. The observed Faraday rotation may be caused not only by the RIAF-like accretion flow but the dense gas localized at the hotspot (hereafter we call it the gas clump). The observed RM toward the hotspot can be preferentially larger if the line of sight to the hotspot intercepts the gas clump (see Figure 3(iii)). As a result, the RM difference between the hotspot and the inner jet can be smaller. We consider that Figure 3(iii) is the most likely scenario to explain the observed RM in NGC 1275 with the CARMA, SMA, and VLBA. This idea is also supported by the movement of the hotspot, which is probably caused by the inhomogeneous ambient medium, as we discussed in Section 4.1. Thus, we consider that the gas clump at the vicinity of the hotspot is the most likely scenario to explain the RM observed with the VLBA. We note that such a clumpy/inhomogeneous ambient medium is also favored by the evidence of the intermittent jet activity (Asada et al. 2006; Nagai et al. 2010). Recent numerical simulations showed that the accretion flow can be unstable because of the thermal instability in the strong X-ray field by the central source and forms cold clumps and filamentary structures on subparsec–parsec scales (Barai et al. 2012; Gaspari et al. 2013). As a result, the accretion flow within the parsec scale cannot be spherical inflow. Although the magnitude of RMs is lower than this value, a relatively high RM is also detected in a small area of jets in a few other radio galaxies (e.g., Gómez et al. 2000; Zavala & Taylor 2002) and attributed to the dense ionized gas in the vicinity of the radio jet.

Here we discuss the properties of this dense gas clump. Since the hotspot is a quite compact feature on the eastern limb, the

interaction between the jet and gas clump should take place in a small area of the jet cross section. Thus, the clump size would be an order of the limb width, say 0.1 mas (0.034 pc). Fujita & Nagai (2017) discussed the density of the surrounding medium in the direction of the jet based on the argument of the momentum balance along the jet. The derived electron density (n_e) is 8.1 cm^{-3} on parsec scales. To account for the observed RM of $\sim 6 \times 10^5$ rad m^{-2} with this electron density, the ambient medium is required to have the magnetic field (B) of 2.7 G, which is much higher than the equipartition magnetic field ($B_{eq} = 4(\pi n_e k_B T)^{0.5}$, where k is a Boltzmann constant) of ~ 24 μG, with the path length of 0.034 pc. Instead, the magnetic field becomes close to the equipartition if we adopt $n_e = 2 \times 10^4$ cm^{-3} ($B \sim B_{eq} = 1.2$ mG). Thus, we conclude that the gas clump has n_e of three orders of magnitude higher than the mean n_e on parsec scales. Such a n_e is consistent with the cloud of the narrow emission line region around the central engine (Osterbrock 1991). It is possible that the gas clump is accreting to the SMBH since it is located within the Bondi radius of 8.6 pc (Fujita et al. 2016).

As we showed in Section 3, the observed RM looks slightly time variable. This could indicate that the gas density is inhomogeneous even within a clump, which causes temporal variations of RM as the hotspot moves. Alternatively, the time variability of RM could be caused by the accretion flow itself. Pang et al. (2011) predicted temporal RM variations due to the dynamical fluctuations of electron density and magnetic field in the accretion flow on the timescale of weeks to years by numerical simulations. They suggested that the RM variations can be a tool to distinguish the accretion flow models. The predominant component of rapid RM variations, however, is the electrons in the vicinity of radius where the electron becomes the relativistic regime (r_{rel}). The radius r_{rel} is expected to be an order of $100R_s$ (Yuan et al. 2003) or even smaller (see discussion by Kuo et al. 2014). Since our measured RM originates in a region much further away, the accretion flow may not be responsible for the observed RM variations. Further observations of RM variations will be valuable to constrain the origin of RM.

4.3. Implications to Magnetic Field Configuration

The energy transport and dissipation mechanism from AGN to cluster scale is the primary subject for the heating of the intra-cluster medium (ICM) against the radiative cooling at the cluster core (e.g., McNamara & Nulsen 2007). Many different heating mechanisms such as the dissipation of sound waves and weak shocks (Fabian et al. 2003, 2005), magnetohydrodynamic (MHD) waves (Fujita et al. 2007), cosmic rays (Fujita & Ohira 2012, 2013), and the mixing of hot bubble gas with the ICM (Hillel & Soker 2017) have been proposed. The magnetic field at the cluster core is crucial for these arguments since the energy transportation can depend on the global configuration of the magnetic field. It is worth noting that all RMs reported in the present paper, Taylor et al. (2006), and Plambeck et al. (2014) show the plus sign, which indicates that the mean line-of-sight magnetic field component points to the observer at three different distances from the central black hole. This allows us to speculate that the magnetic field configuration in the ambient medium is radial from the black hole to ~ 8 pc scale. The RM toward the counter jet component would show a minus sign if this is the case. Measurements of the RM toward the counter jet are key to test this speculation. A counter jet component N1 reported in Fujita & Nagai (2017) is possibly a hotspot interacting with the ambient medium. A relatively ordered magnetic field is likely to exist in such a region. Thus, the polarized emission can be detected from this component by higher-frequency VLBI observations, which can avoid a strong FFA and Faraday depolarization by the accretion disk (e.g., Walker et al. 2000).

As we discussed in Section 4.2, the equipartition magnetic field on parsec scales is estimated to be about 24 μG. If the magnetic field configuration is radial ($B(r) \propto r^{-2}$), the magnetic field strength should be 1.6×10^4 G at $\sim 1R_S$. We note that the accretion flow can be inhomogeneous (see the discussion in Section 4.2), which is likely to cause changes in the magnetic field direction. Thus, this is the first-order approximation. There is no measurement of the magnetic field strength at the vicinity of the SMBH for 3C 84, so it is not possible to do a comparison of the derived value with a different approach. One relevant piece of information is that Kino et al. (2015) derived the magnetic field strength of about 100 G at the base of the jet of M87 using the turnover frequency due to the synchrotron self-absorption with the aid of Event Horizon Telescope (EHT) data. This value is somewhat smaller than the case of 3C 84, but the magnetic field of 3C 84 can be much larger than M87 since the radio luminosity of 3C 84 is roughly two orders of magnitude larger than that of M87. O'Sullivan & Gabuzda (2009) estimated the magnetic field strength at the jet base for BL Lac objects using the core-shifts argument and derived an order of 10^4 G, which is similar to our estimate for 3C 84. It seems that the radial configuration of magnetic field in the ambient medium is not too extreme of an assumption.

4.4. Implications to the Origin of Low Polarization in 3C 84

Traditionally, 3C 84 is used as an instrumental polarization calibrator for most VLA frequencies and configurations because no strong polarized emission is detected. In the image presented in this paper, the polarized emission is detected as a spot while the emissions from the remaining regions are indeed unpolarized. This might indicate that the magnetic field of the ambient medium is highly turbulent within the VLBA beam size (~ 0.3 mas $\simeq 0.1$ pc), resulting in a strong depolarization, and the magnetic field is somehow ordered only in the vicinity of the hotspot. If this is the case, the jet may not be interacting with a 'clumpf but a stretched or filamentary gas feature supported by the ordered magnetic field. Such a gas feature could be a scaled-down version of the Hα filaments observed in kiloparsec to 10 kpc scales (Fabian et al. 2008). However, we cannot exclude a possibility that the emissions from the jet of 3C 84 are intrinsically less polarized. It is noteworthy that not only 3C 84 but also other radio galaxies (M87, Cen A, Cyg A) show no or little polarization (Middelberg et al. 2005) in contrast to strongly polarized jets of blazars. Interestingly, all these radio galaxies show a limb-brightened structure (M87: Kovalev et al. 2007; Ly et al. 2007; Hada et al. 2011, Cen A: Kataoka et al. 2006, Cyg A: Boccardi et al. 2016), which is suggestive of the velocity gradient across the jet width. The number of studies on the spectral energy distribution of AGN jets also support this model (e.g., Ghisellini et al. 2005; Tavecchio & Ghisellini 2008, 2014). The observed difference in the polarized emission between blazars and radio galaxies can be explained if the spine emission is strongly polarized while the sheath emission is less polarized. This scenario can

be testable with millimeter and submillimeter VLBI observations with the Global Millimeter VLBI Array (GMVA) and the EHT with the Atacama Large Millimeter/submillimeter Array (Array), which are less affected by the depolarization thanks to small beam and high frequency.

We thank an anonymous referee for constructive comments that improved the manuscript. This study makes use of 43 GHz VLBA data from the VLBA-BU Blazar Monitoring Program (VLBA-BU-BLAZAR; http://www.bu.edu/blazars/VLBAproject.html), funded by NASA through the Fermi Guest Investigator Program. H.N. acknowledges S. Jorstad for providing the detail of calibrations for BU data and useful discussions. The VLBA is an instrument of the National Radio Astronomy Observatory. The National Radio Astronomy Observatory is a facility of the National Science Foundation operated by Associated Universities, Inc. H.N. is supported by MEXT KAKENHI Grant Number 15K17619. Y.F. is supported by MEXT KAKENHI Grant Number 15K05080.

ORCID iDs

H. Nagai https://orcid.org/0000-0003-0292-3645
Y. Fujita https://orcid.org/0000-0003-0058-9719
M. Nakamura https://orcid.org/0000-0001-6081-2420

References

Asada, K., Kameno, S., Shen, Z.-Q., et al. 2006, PASJ, 58, 261
Barai, P., Proga, D., & Nagamine, K. 2012, MNRAS, 424, 728
Begelman, M. C., & Cioffi, D. F. 1989, ApJL, 345, L21
Boccardi, B., Krichbaum, T. P., Bach, U., Bremer, M., & Zensus, J. A. 2016, A&A, 588, L9
Dutson, K. L., Edge, A. C., Hinton, J. A., et al. 2014, MNRAS, 442, 2048
Fabian, A. C., Johnstone, R. M., Sanders, J. S., et al. 2008, Natur, 454, 968
Fabian, A. C., Reynolds, C. S., Taylor, G. B., & Dunn, R. J. H. 2005, MNRAS, 363, 891
Fabian, A. C., Sanders, J. S., Allen, S. W., et al. 2003, MNRAS, 344, L43
Fabian, A. C., Walker, S. A., Pinto, C., Russell, H. R., & Edge, A. C. 2015, MNRAS, 451, 3061
Fanaroff, B. L., & Riley, J. M. 1974, MNRAS, 167, 31P
Fujita, Y., Kawakatu, N., Shlosman, I., & Ito, H. 2016, MNRAS, 455, 2289
Fujita, Y., & Nagai, H. 2017, MNRAS, 465, L94
Fujita, Y., & Ohira, Y. 2012, ApJ, 746, 53
Fujita, Y., & Ohira, Y. 2013, MNRAS, 428, 599
Fujita, Y., Suzuki, T. K., Kudoh, T., & Yokoyama, T. 2007, ApJL, 659, L1
Gaspari, M., Ruszkowski, M., & Oh, S. P. 2013, MNRAS, 432, 3401
Ghisellini, G., Tavecchio, F., & Chiaberge, M. 2005, A&A, 432, 401
Gómez, J.-L., Marscher, A. P., Alberdi, A., Jorstad, S. G., & Agudo, I. 2002, VLBA Scientific Memo No. 30
Gómez, J.-L., Marscher, A. P., Alberdi, A., Jorstad, S. G., & García-Miró, C. 2000, Sci, 289, 2317
Hada, K., Doi, A., Kino, M., et al. 2011, Natur, 477, 185
Hillel, S., & Soker, N. 2017, MNRAS, 466, L39
Ho, L. C. 2008, ARA&A, 46, 475
Ichimaru, S. 1977, ApJ, 214, 840
Jorstad, S. G., Marscher, A. P., Lister, M. L., et al. 2005, AJ, 130, 1418
Kataoka, J., Stawarz, Ł., Aharonian, F., et al. 2006, ApJ, 641, 158
Kino, M., Takahara, F., Hada, K., et al. 2015, ApJ, 803, 30
Kovalev, Y. Y., Lister, M. L., Homan, D. C., & Kellermann, K. I. 2007, ApJL, 668, L27
Kuo, C. Y., Asada, K., Rao, R., et al. 2014, ApJL, 783, L33
Laing, R. A. 1980, MNRAS, 193, 439
Levinson, A., Laor, A., & Vermeulen, R. C. 1995, ApJ, 448, 589
Lim, J., Ao, Y., & Dinh-V-Trung 2008, ApJ, 672, 252
Liu, B. F., & Taam, R. E. 2013, ApJS, 207, 17
Liu, B. F., Taam, R. E., Meyer-Hofmeister, E., & Meyer, F. 2007, ApJ, 671, 695
Lobanov, A. P. 1998, A&AS, 132, 261
Ly, C., Walker, R. C., & Junor, W. 2007, ApJ, 660, 200
Marrone, D. P., Moran, J. M., Zhao, J.-H., & Rao, R. 2006, ApJ, 640, 308
McNamara, B. R., & Nulsen, P. E. J. 2007, ARA&A, 45, 117
Merloni, A., & Fabian, A. C. 2002, MNRAS, 332, 165
Middelberg, E., Roy, A. L., Bach, U., Gabuzda, D. C., & Beckert, T. 2005, in ASP Conf. Proc. 340, Future Directions in High Resolution Astronomy: The 10th Anniversary of the VLBA, ed. J. Romney & M. Reid (San Francisco, CA: ASP), 189
Miller, K. A., & Stone, J. M. 2000, ApJ, 534, 398
Nagai, H., Haga, T., Giovannini, G., et al. 2014, ApJ, 785, 53
Nagai, H., Suzuki, K., Asada, K., et al. 2010, PASJ, 62, L11
Narayan, R., & Fabian, A. C. 2011, MNRAS, 415, 3721
Narayan, R., Igumenshchev, I. V., & Abramowicz, M. A. 2000, ApJ, 539, 798
Narayan, R., & Yi, I. 1995, ApJ, 444, 231
Osterbrock, D. E. 1991, RPPh, 54, 579
O'Sullivan, S. P., & Gabuzda, D. C. 2009, MNRAS, 400, 26
Pang, B., Pen, U.-L., Matzner, C. D., Green, S. R., & Liebendörfer, M. 2011, MNRAS, 415, 1228
Perlman, E. S., Mason, R. E., Packham, C., et al. 2007, ApJ, 663, 808
Plambeck, R. L., Bower, G. C., Rao, R., et al. 2014, ApJ, 797, 66
Quataert, E., & Gruzinov, A. 2000, ApJ, 545, 842
Romney, J. D., Benson, J. M., Dhawan, V., et al. 1995, PNAS, 92, 11360
Salomé, P., Combes, F., Edge, A. C., et al. 2006, A&A, 454, 437
Scharwächter, J., McGregor, P. J., Dopita, M. A., & Beck, T. L. 2013, MNRAS, 429, 2315
Shakura, N. I., & Sunyaev, R. A. 1973, A&A, 24, 337
Shepherd, M. C., Pearson, T. J., & Taylor, G. B. 1994, BAAS, 26, 987
Silver, C. S., Taylor, G. B., & Vermeulen, R. C. 1998, ApJ, 502, 229
Sokolovsky, K. V., Kovalev, Y. Y., Pushkarev, A. B., & Lobanov, A. P. 2011, A&A, 532, A38
Sosa-Brito, R. M., Tacconi-Garman, L. E., Lehnert, M. D., & Gallimore, J. F. 2001, ApJS, 136, 61
Suzuki, K., Nagai, H., Kino, M., et al. 2012, ApJ, 746, 140
Tan, J. C., Beuther, H., Walter, F., & Blackman, E. G. 2008, ApJ, 689, 775
Tavecchio, F., & Ghisellini, G. 2008, MNRAS, 385, L98
Tavecchio, F., & Ghisellini, G. 2014, MNRAS, 443, 1224
Taylor, G. B., Gugliucci, N. E., Fabian, A. C., et al. 2006, MNRAS, 368, 1500
Taylor, G. B., & Vermeulen, R. C. 1996, ApJL, 457, L69
Vaillancourt, J. E. 2006, PASP, 118, 1340
Wagner, A. Y., Bicknell, G. V., & Umemura, M. 2012, ApJ, 757, 136
Walker, R. C., Dhawan, V., Romney, J. D., Kellermann, K. I., & Vermeulen, R. C. 2000, ApJ, 530, 233
Yuan, F., Quataert, E., & Narayan, R. 2003, ApJ, 598, 301
Zavala, R. T., & Taylor, G. B. 2002, ApJL, 566, L9